Digest Journal of Nanomaterials and Biostructures Vol. 7, No. 3, July - September 2012, p. 917 - 932

OBTAINING AND CHARACTERIZATION OF HA/Y_2O_3:αAl_2O_3 SYSTEM FOR BIOAPPLICATIONS

I. MERCIONIU*, G. E. STAN, R. BERCIA[a], S. CIUCA[a],
N. POPESCU-POGRION
National Institute of Materials Physics, Magurele, Romania
[a]*University POLITEHNICA of Bucharest, Bucharest, Romania*

A new HA/Y_2O_3:αAl_2O_3 system was obtained by the deposition of a hydroxyapatite thin layer (~150 nm), by magnetron sputtering, onto sintered substrates of low yttria (150 ppm) doped alumina. The yttria doped alumina was synthesized from very pure nanopowders, by mechanical homogenization, followed of pressing, sintering and different annealing regimes, in order to obtain bodies with various degree of nano-micro-structuration. TEM/ HRTEM, SEM and EDS morpho-compositional analysis techniques were used to characterize the yttria doped alumina substrate and the hydroxyapatite superficial layer. The interfacial bonding strength between the sintered substrate and the hydroxyapatite thin film was analyzed by SEM. The evolution of the grains growth of the Y_2O_3:αAl_2O_3 substrate samples, with and without the hydroxyapatite covering layer is observed and discussed. A strong structural interdependence between the covering layer and the sintered substrate was emphasized. The grains' growth behaviour of the studied samples showed a linear evolution. A mathematical model for the grain growth process description was built, the grain size being interpreted as a random variable having a log-normal or Weibull probability density function.

(Received December 22, 2012; Accepted June 28, 2012)

Keywords: hydroxyapatite, Y_2O_3 doped αAl_2O_3, mathematical model

1. Introduction

Ceramic biomaterials are commonly classified, by their chemical stability *in vitro/in vivo* and by the specific biological response elicited during prolonged contact, in: inert (alumina, zirconia), surface reactive [hydroxyapatite (HA, $Ca_{10}(PO_4)_6(OH)_2$), bioglasses, glass ceramics] and resorbable (tricalcium phosphates, polylactic acid, polyglycolic acid) [1]. During the last decades their medical application has been extending progressively, covering nowadays an important realm, from orthopaedics, maxillofacial surgery and dentistry to heart or even cranial reconstruction surgery [2].

Since 1975, when its bio-inertness was demonstrated, alumina (especially the αAl_2O_3 form) shown a great potential for medicine [3]. In 2002 Noiri et al. [4] evaluated histopathalogically the biocompatibility of alumina-ceramic materials for eight weeks, by the implantation in the eye sockets of albino rabbits. The results showed no signs of implant rejection or prolapse. Since then the biocompatibility of alumina (in amorphous or crystalline form) has been tested and proven by many researchers [5,6]. Moreover, the alumina's excellent mechanical properties (e.g.: high hardness and high abrasion resistance) made this material an important and safe choice in many load-bearing implant applications [2].

Recently, a growing interest of the biomedical community for doped αAl_2O_3 materials has been noticed, due to their superior mechanical and biological properties [2,7,8]. For instance, yttria (Y_2O_3) doped alumina is known to have up to two orders of magnitude better mechanical

*Corresponding author: imercioniu@infim.ro

properties than pure αAl_2O_3 [8,9]. The improvement of the yttria doped alumina mechanical properties is attributed to a suppression of grain boundary diffusion [10].

In case of sintered materials, the micro-structural evolution depends on the characteristics of the starting powders (e.g.: particles' shape, agglomeration, average size and dimensional distribution), and on the sintering and coarsening processes. The physical-chemical state of the powder (especially the microstructure, geometrical shape, average dimension and porosity) is a complex criterion, very important for the technological parameters, theoretical studies, and characterization of the samples after pressing (green bodies) or after sintering and stabilization of the chemical composition stoichiometry.

The special structural characteristics (e.g.: porosity, grains' shape and average size) of the final products (resulted sintered bodies) determine the desired material's properties. When doping material is added, the doping ions may react with the major constituents and may be redistributed for thermodynamic or kinetic reasons. Impurities (intentional doping and/or contamination) could have a dramatic effect on the microstructural evolution, sintering and physical properties of the polycrystalline αAl_2O_3 [8–13].

This study introduce a new bioceramic system: *low yttria (150ppm) doped* αAl_2O_3 (denoted further on: *150Y:*αAl_2O_3), functionalized by depositing on its surface a *bioactive thin layer of hydroxyapatite*.

The deposition method selected for the synthesis of the HA thin films was Radio-Frequency Magnetron Sputtering (RF-MS). RF-MS is a very powerful deposition technique, which is used in a wide range of applications, due to its excellent control over thickness and uniformity, excellent adherence of the films and its versatility in automatization [14,15].

Despite the large number of articles on the low yttrium doped αAl_2O_3 sintering stability and grain growth's dependence of the annealing parameters [16,17], some fundamental questions remain open. Most of these studies mainly dealt with the influence of small level of impurities at the grain boundary and the grain growth mechanism of the materials during annealing treatment.

It is expected that the geometry, average size, homogeneity of 150Y:αAl_2O_3 particles will determine the structural characteristics of the compact specimens, such as shape, size and average size of the grains, grain boundaries, surface and interface state, porosity, and crystalline phases.

In this paper, we focus on the 150Y:αAl_2O_3 grains' growth behaviour dependence on the sintering and annealing conditions; the growth rates and the grain size distributions being as well emphasized along with the substrates' relationships with the top HA layer. Mathematical models for the grain growth processes' description were tested and their results are presented and discussed.

2. Experimental

2.1 *Sample preparation*

2.1.1 Yttria doped αAl_2O_3

Yttria (150ppm) doped αAl_2O_3 (150Y:αAl_2O_3) ceramics were prepared from high purity nanocrystalline αAl_2O_3 (nominal purity of 99.85%) and Y_2O_3 (nominal purity of 99.95%) powders produced by INFRAMAT - USA. The powders were ball-milled for 1 h in isopropyl alcohol. High purity alumina ball were used. Milled powders were dried on a hot plate and lightly ground in an agate mortar. 8–10 mm thick green bodies were obtained by uniaxially pressing in a 13 mm diameter stainless-steel die. To minimize contamination during sintering, the samples were placed in a bed of alumina powder, having the same composition as the starting powder, inside the crucible, and covered with a second crucible [9]. We used the sintering algorithms described in *Ref.9*. The samples were calcined for 2 hours at 1100°C (using a heating rate, between 25°C – 1100°C, of 5°C/min) and then sintered for 2.5 hours at 1550°C (using a heating rate, between 1100°C – 1550°C, of 10°C/min). The cooling rate was 38°C/min. After sintering, the samples

were subjected to a series of annealing treatments performed at T_a=1650°C for different periods of time (t = 2, 4, 6, 8, 10, 12, 14 hours).

2.1.2 Hydroxyapatite thin films' deposition

The HA cathode target (110 mm diameter, 3 mm thick) was manufactured by cold pressing from high purity $Ca_{10}(PO_4)_6(OH)_2$ powder (Sigma Aldrich). An additional Al_2O_3 target (Sigma Aldrich), prepared in similar conditions, was used for the co-sputtering deposition experiments. We used as deposition substrates 150Y:αAl_2O_3 rectangular pieces synthesised in the conditions presented at 2.1.1. Prior to deposition the substrates were ultrasonically cleaned successively in acetone and then isopropyl alcohol for 10 minutes. The substrates were finally dried in nitrogen flow and fixed on the aluminium holders of the deposition system.

The films were prepared using an UVN-75R1 sputtering deposition system having a magnetron planar cathode with a plasma ring of ~55 mm diameter, operating at radio-frequency of 1.78 MHz. In the first step the working chamber was evacuated down to a residual pressure of 10^{-3} Pa. Further on, high purity argon (99.999%) was introduced through a needle valve and the gas flow was maintained at a value of 45 sccm. The target to substrate distance was set at 35 mm. All deposition were carried out at 0.4 Pa working pressure, as measured by a capacitive gauge (Alcatel ASD 1004). To improve the adhesion at the alumina – hydroxyapatite interface, we first synthesized a buffer layer with gradient composition. The graded buffer layer $(Al_2O_3)_x(HA)_{1-x}$ (x=0–1) was prepared by co-sputtering, slowly moving the rotating substrate holder from the Al_2O_3 target towards the HA target [18–20]. By this procedure a functionally graded transition zone with variable chemical composition can be formed between the alumina-based substrate and the top biofunctional HA coating. This process lasted 120 min, the graded layer thickness being estimated at around ~140 nm. Finally, the Al_2O_3 target cathode was shut down and the described functional graded structures were placed for 80 min in front of the HA target in order to prepare a biofunctional top HA layer having a thickness of ~150 nm. During the magnetron sputtering process the substrates' temperature reached a maximum of ~200°C, as estimated by a built-in temperature controller. No post-deposition heat-treatments were applied.

2.1.3 Sample preparation for statistical investigations and mathematical model

The Transmission Electron Microscopy/High Resolution Transmission Electron Microscopy (TEM/HRTEM) studies were carried out using a JEOL JEM ARM 200F apparatus, at an accelerating voltage of 200 kV. The TEM/HRTEM samples were prepared by dipping the 3 mm holey carbon grids into ultrasonically dispersed oxide powder in ethyl alcohol.

The cross-sectional view Scanning Electron Microscopy (SEM) investigations were performed using a TESCAN microscope (model Lyra3XMU dual SEM-FIB system) at an accelerating voltage of 5kV, while the top-view analyses were carried out on a FEI QUANTA microscope at an accelerating voltage of 30 kV. The cross-sectional view SEM characterizations were realized on thin slices cut perpendicular to the sample axis. After cutting, the sintering body was placed in the oven for another annealing stage at T_a=1650°C. Prior to all SEM micro-structural analyses the 150Y:αAl_2O_3 samples were coated with a thin conductive (gold) layer.

Grain sizes were measured on SEM images, each containing 50–100 grains. Statistical analysis on the experimental data was performed. Mean grains' size and size distribution was determined by statistical interpretations (around 1000 grains were measured for each slice). In order to check for the experimental reproducibility, the analyses were performed on duplicate samples (denoted further on: *150Y:αAl_2O_3-**I*** and *150Y:αAl_2O_3-**II***), prepared and annealed in identically conditions. Both sets of results are presented comparatively in this study.

3. Results and Discussion

3.1 TEM investigation of 150Y:αAl$_2$O$_3$ nanopowders

TEM/HRTEM images, depicting the 150Y:αAl$_2$O$_3$ nanopowder's structure, are shown in Figure 1.

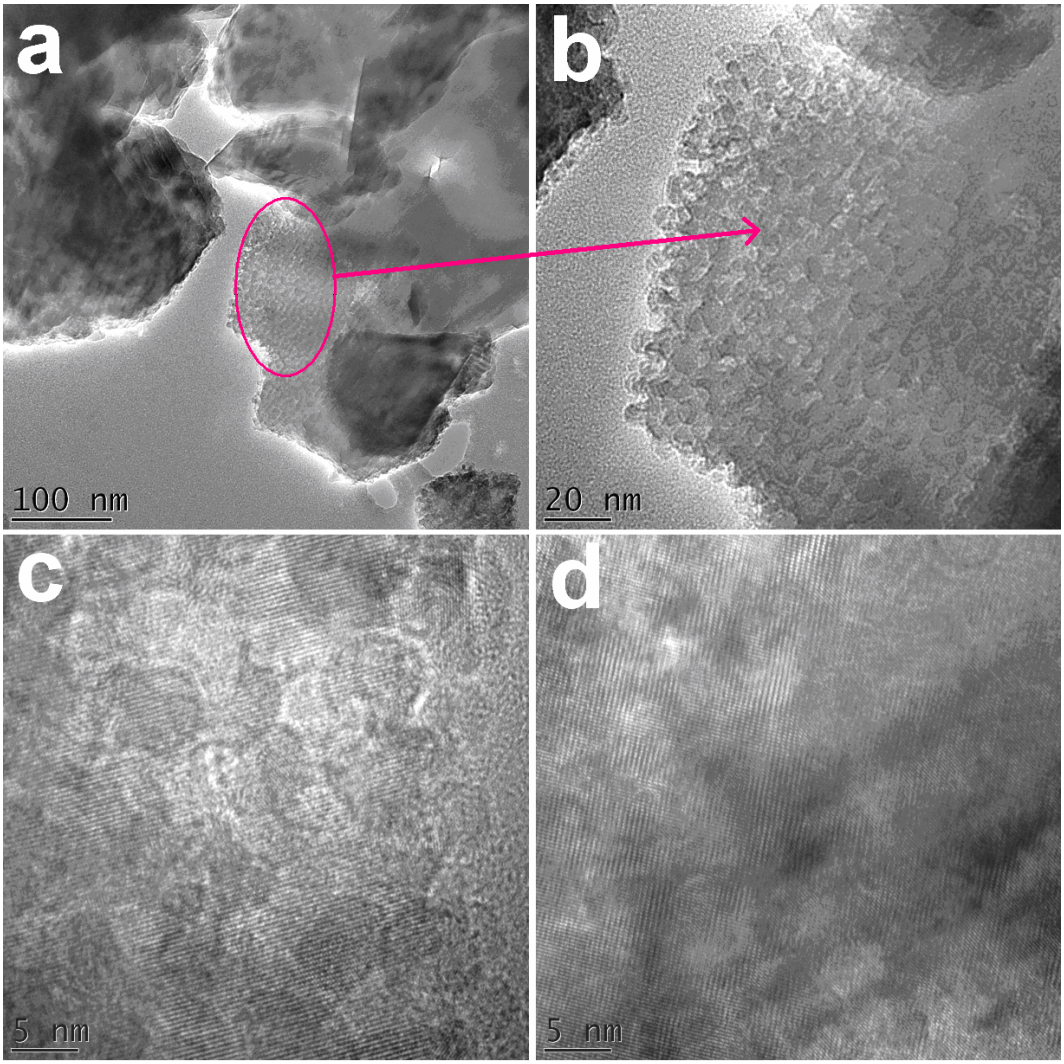

Fig. 1. TEM images (a – general view; b – detail view) and HRTEM images for 150Y:αAl$_2$O$_3$ nanopowder sample.

3.2 SEM-EDS investigations of the HA/150Y:αAl$_2$O$_3$ system

The cross-sectional view SEM images are shown in Figure 2a (*microstructure of the 150Y:αAl$_2$O$_3$ substrate*) and Figure 3a (*display of the HA/150Y:αAl$_2$O$_3$ interface*). Figure 4a presents the top-view morphology of the HA top biofunctional film. One can notice the intimate bonding between the HA layer (having a thickness in range of 110 – 200 nm) and the 150Y:αAl$_2$O$_3$ (Figure 3a), the HA film closely mimicking the substrate relief (Figure 3a and 4a), covering it entirely. No cracks or delamination phenomena were observed at the interface (Figure 3a). The EDS spectra corresponding to each area of SEM analysis are displayed in Figures 2b, 3b,b' and 4b, respectively. No impurities were detected in both substrates and films.

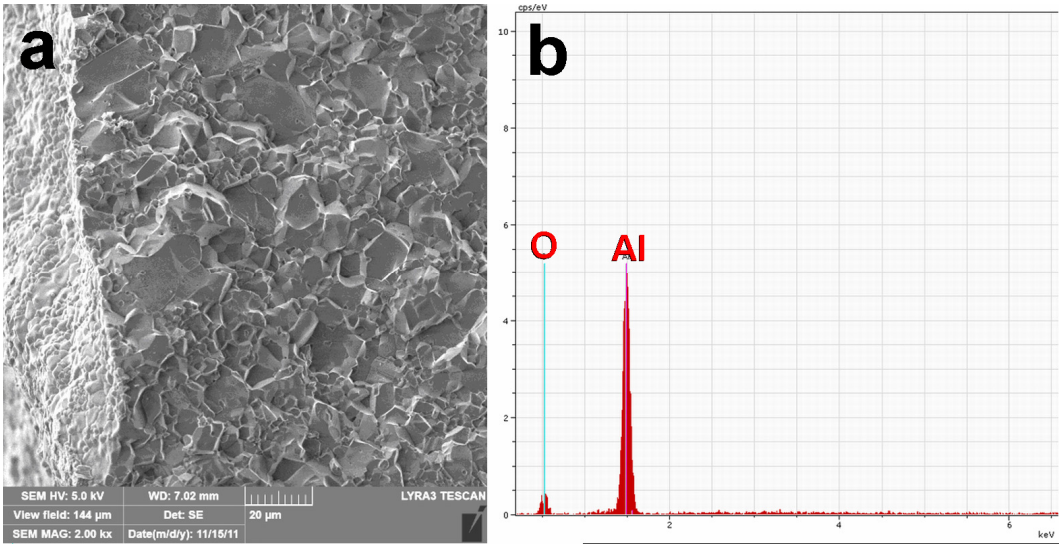

Fig 2. Cross-sectional SEM image (a) and corresponding EDS spectrum (b) for the 150Y:αAl_2O_3 substrate.

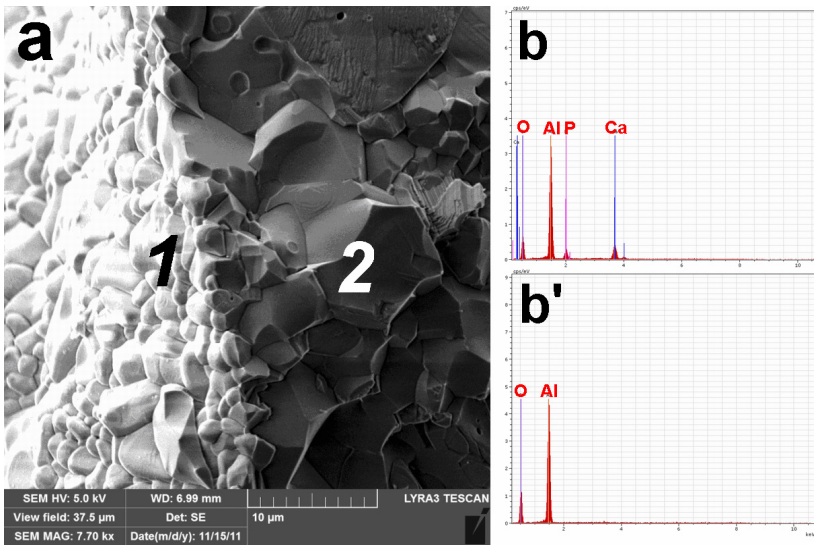

Fig 3. Cross-sectional SEM image of the HA/150Y:αAl_2O_3 interface (a) and corresponding EDS spectra performed in points 1 (b) and 2 (b') of the SEM image.

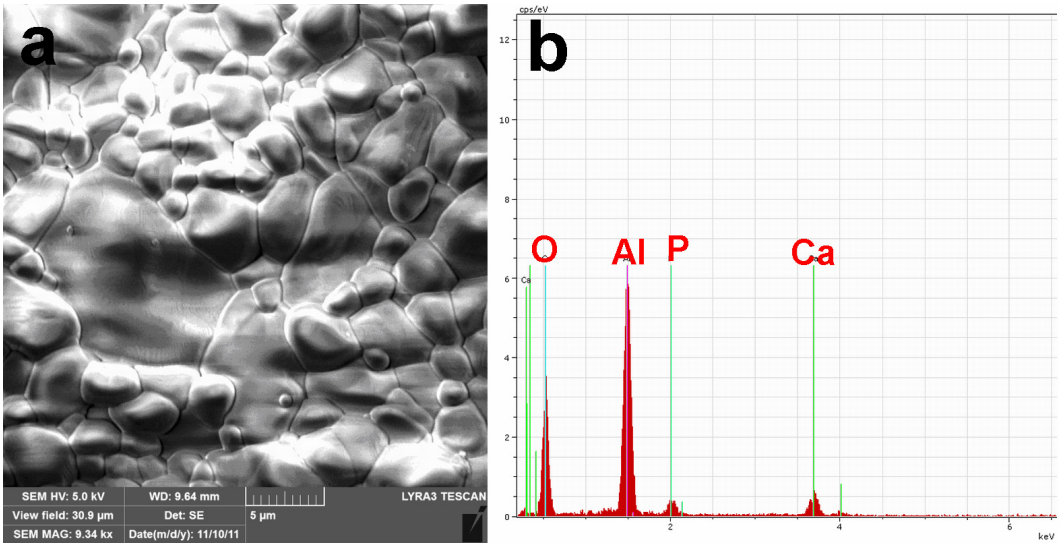

Fig 4. Top-view SEM image (a) and corresponding EDS spectrum (b) for HA film.

3.3 The grain growth dependence of the annealing times – statistical interpretations

Both sets of samples **(**150Y:αAl_2O_3-**I** and 150Y:αAl_2O_3-**II)** had a good densification (low porosity) after the annealing treatments performed at T_a =1650°C, for different periods of time (t= 2 ÷ 14 h) (Figures 5 and 6). No abnormal grain growth (AGG) was observed. One can notice a similar evolution of the grain growth (GG) processes for both 150Y:αAl_2O_3-**I**, 150Y:αAl_2O_3-**II** sets of sample (see Figures 5 and 6).

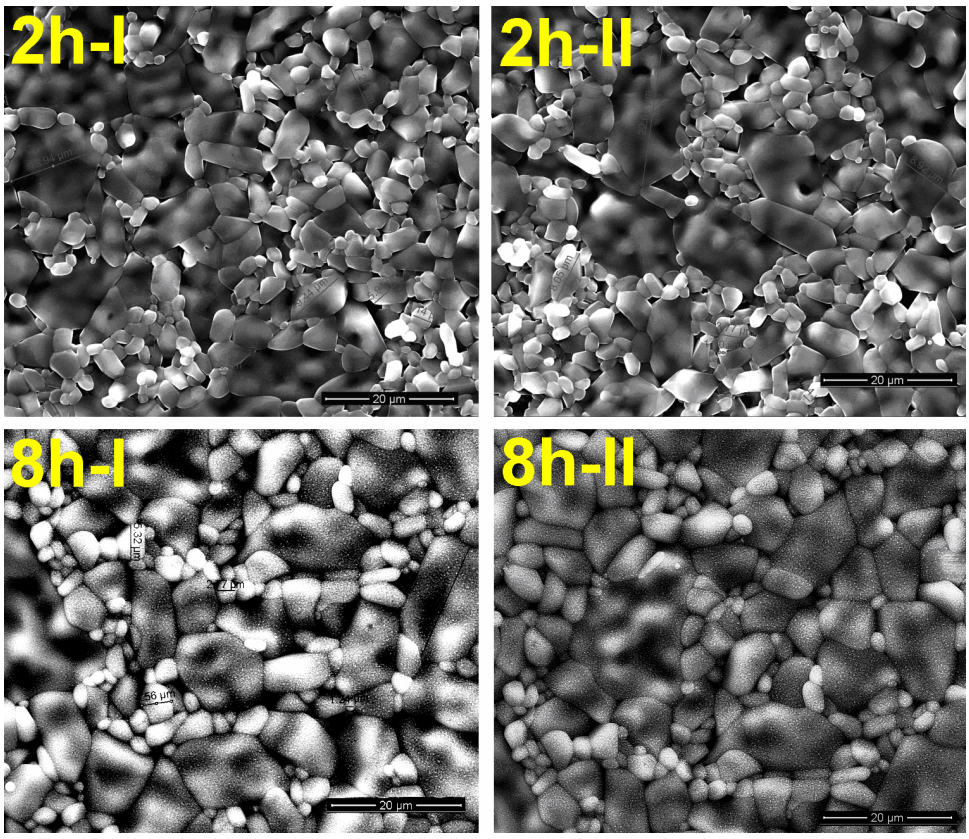

*Fig. 5. Top-view SEM images for the 150Y_2O_3:αAl_2O_3-I (left side) and 150Y_2O_3:αAl_2O_3-II (right side) samples, subjected to annealing treatments at 1650°C for **2 h** and **8 h**, respectively.*

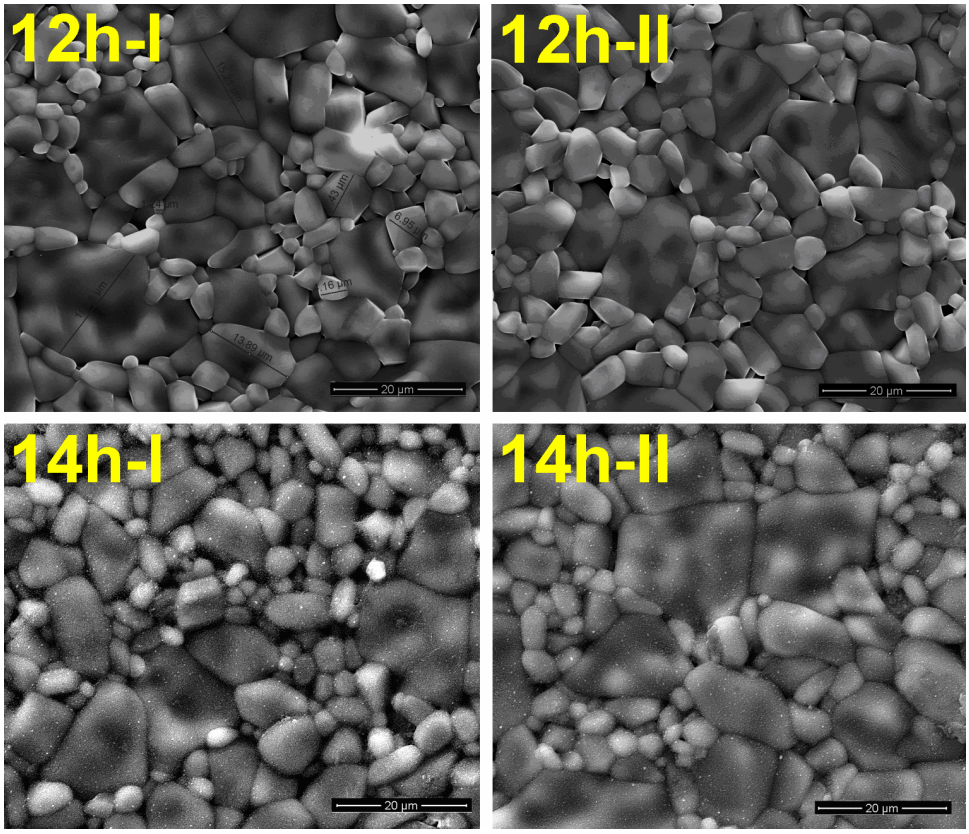

*Fig. 6 Top-view SEM images for the 150Y_2O_3:αAl_2O_3-I (left side) and 150Y_2O_3:αAl_2O_3-II (right side) samples, subjected to annealing treatments at 1650°C for **12 h** and **14 h**, respectively.*

3.3.1 Statistical description of the samples

From Figures 5 and 6 were extracted morphological parameters of the samples, such as grains' shape, porosity, dimensional value of the average grain, or the dimensional range of the grains. Statistical interpretations have been performed, the histograms of the grains' sizes for the samples analyzed after t = 2, 4, 6, 8, 10, 12, 14 h are presented in Figures 7 – 13.

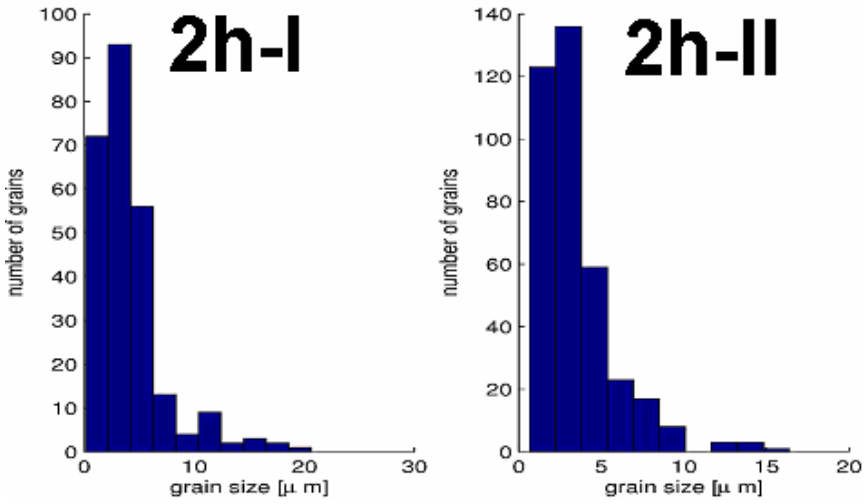

*Fig. 7. Histograms of grains' sizes at **t=2h** for sample set I (left side) and sample set II (right side).*

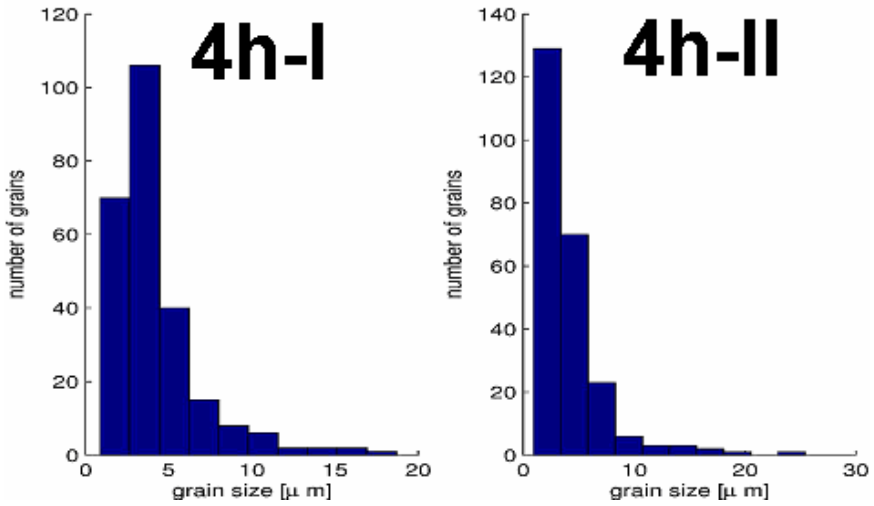

*Fig. 8. Histograms of grains' sizes at **t=4h** for sample set I (left side) and sample set II (right side).*

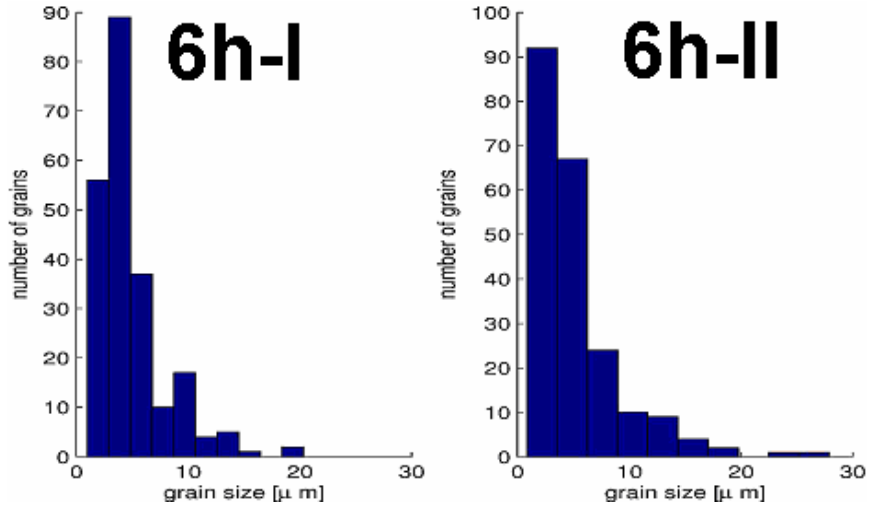

*Fig. 9. Histograms of grains' sizes at **t=6h** for sample set I (left side) and sample set II (right side).*

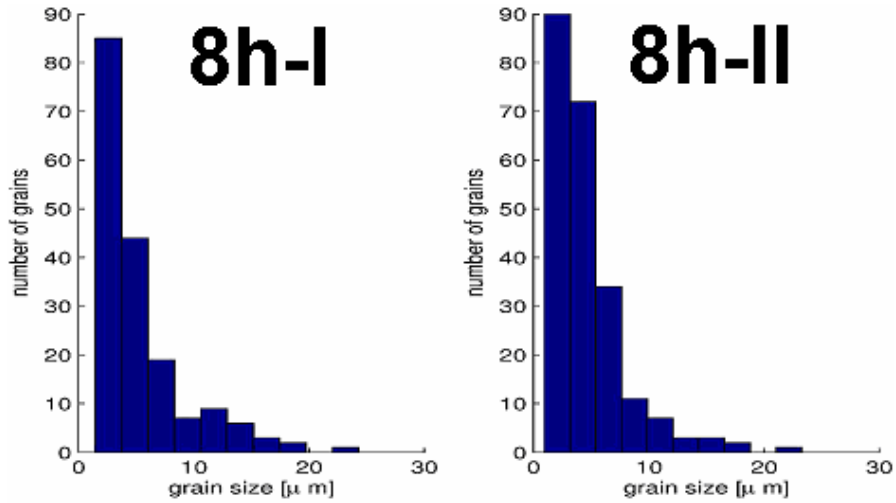

*Fig. 10. Histograms of grains' sizes at **t=8h** for sample set I (left side) and sample set II (right side).*

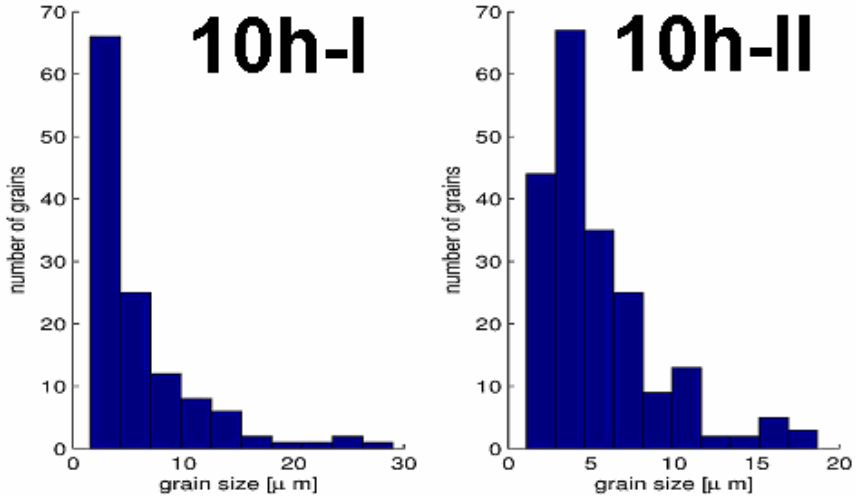

*Fig. 11. Histograms of grains' sizes at **t=10h** for sample set I (left side) and sample set II (right side).*

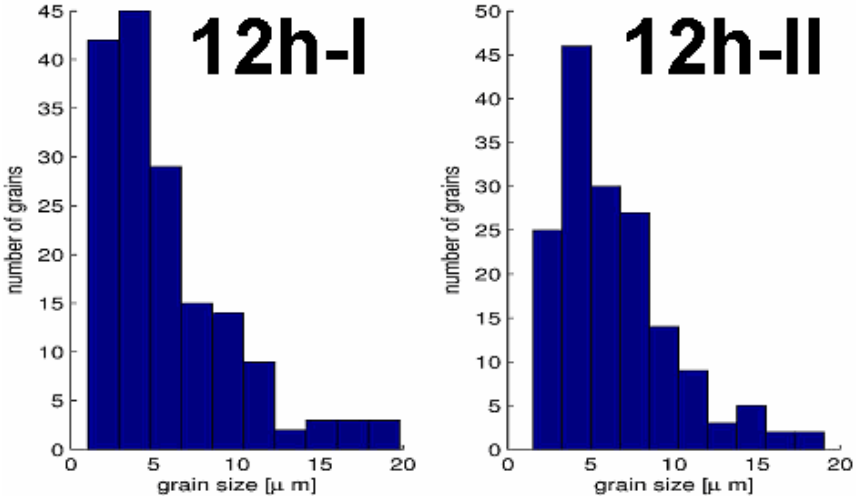

*Fig. 12. Histograms of grains' sizes at **t=12h** for sample set I (left side) and sample set II (right side).*

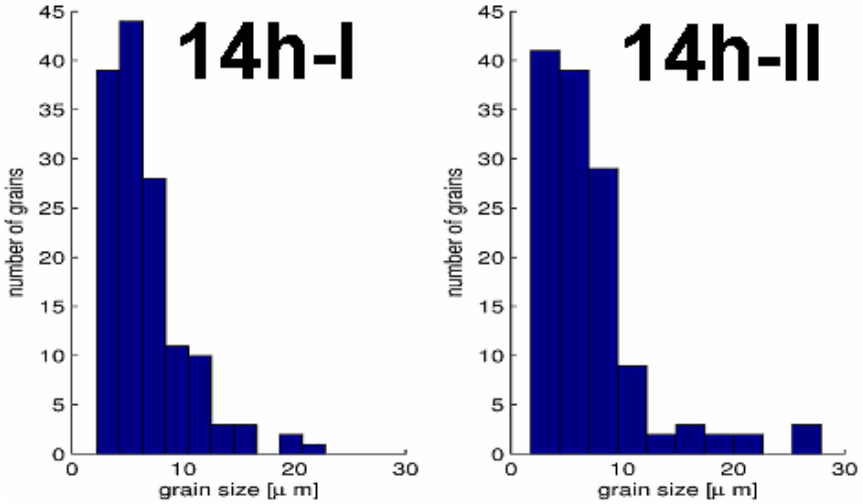

*Fig. 13. Histograms of grains' sizes at **t=14h** for sample set I (left side) and sample set II (right side).*

We calculated the average value $m(X)=\frac{1}{N}\sum_{i=1}^{N}x_i$ and the variance $v(X)=\frac{1}{N}\sum_{i=1}^{N}\left(x_i-m(X)\right)^2$ corresponding to each sample data $X=\{x_i, i=1,2,...,N\}$, e.g. grain sizes at each annealing time *t*. The mean and variance of the grains' size values are presented in Table 1. One can observe that, the mean of the grain size increase in time for both sets of samples. There are more grains with the size smaller than mean value. In the t = 2 ÷ 6 h interval, the distribution of the grains' sizes is concentrated around its mean, while after 6 h of annealing, the distribution of the grains' sizes became less concentrated.

Table 1. Mean and variance of grains' sizes.

	Set I		**Set II**	
Time	**Mean**	**Variance**	**Mean**	**Variance**
2	4.0928	10.0322	3.5245	5.3536
4	4.2210	7.4381	4.1357	9.7873
6	4.8860	9.8860	5.0898	15.8123
8	5.2195	15.6018	4.7234	10.6675
10	6.1591	26.4302	5.4094	12.3418
12	5.8259	15.5592	6.4535	12.1104
14	6.5158	13.3856	7.0103	21.9911

During normal grain growth, the average grain size increases continuously; the grain size distribution being a *normal distribution* (self-similar)/G*aussian distribution*. During abnormal grain growth (AGG) the average grain size will grow in accordance to a bimodal distribution (the self-similarity is lost). Similar trends have been notices also in other studies on doped or impure alumina, or in the special case of low yttria (150 ppm) doped αAl_2O_3 sintered in special conditions [16,17,21,22].

Our qualitative and quantitative statistical analysis suggests that the grain size can be considered as a random variable with log-normal distribution or as a Weibull random variable. Consequently, the GG process will be modelled by a stochastic process.

3.3.2 The log-normal model

One supposes that, the grain size at each moment *t* is a random variable having log-normal probability density function *f*, with parameters μ and σ,

$$f(x;\mu,\sigma)=\frac{1}{x\sigma\sqrt{2\pi}}\exp\left(-\frac{(\ln x-\mu)^2}{2\sigma^2}\right),\quad x>0. \qquad \textbf{Eq.1}$$

For the sample of measured grain sizes $X=\{x_i, i=1,2,...,N\}$, at each moment *t*, we can calculate the maximum likelihood parameter estimators, $\hat{\mu}$ and $\hat{\sigma}$, using the relations:

$$\hat{\mu}=\frac{1}{N}\sum_{i=1}^{N}\ln x_i \text{ and } \hat{\sigma}=\frac{1}{N}\sum_{i=1}^{N}(\ln x_i-\hat{\mu})^2\,. \qquad \textbf{Eq.2}$$

Also, we have determined the 95%-confidence intervals for μ and σ. The calculated values for the two sets of samples are presented in Tables 2 and 3.

Table 2. Maximum likelihood parameter estimators and confidence intervals for sample set I.

	Parameter μ		Parameter σ	
Time	$\hat{\mu}(t)$	**Confidence interval 95%**	$\hat{\sigma}(t)$	**Confidence interval 95%**
2	1.1740	(1.0884 , 1.2596)	0.6942	(0.6387 , 0.7603)
4	1.2849	(1.2181 , 1.3517)	0.5387	(0.4954 , 0.5903)
6	1.4225	(1.3482 , 1.4967)	0.5600	(0.5122 , 0.6177)
8	1.4361	(1.3423 , 1.5299)	0.6304	(0.5707 , 0.7041)
10	1.5741	(1.4569 , 1.6913)	0.6594	(0.5863 , 0.7535)
12	1.5585	(1.4601 , 1.6568)	0.6398	(0.5774 , 0.7174)
14	1.7443	(1.6611 , 1.8275)	0.4997	(0.4474 , 0.5660)

Table 3. Maximum likelihood parameter estimators and confidence intervals for sample set II.

	Parameter μ		Parameter σ	
Time	$\hat{\mu}(t)$	**Confidence interval 95%**	$\hat{\sigma}(t)$	**Confidence interval 95%**
2	1.0895	(1.0313 , 1.1476)	0.5711	(0.5328 , 0.6153)
4	1.2348	(1.1614 , 1.3082)	0.5748	(0.5274 , 0.6317)
6	1.4017	(1.3128 , 1.4906)	0.6535	(0.5964 , 0.7227)
8	1.3810	(1.3070 , 1.4550)	0.5610	(0.5133 , 0.6185)
10	1.5125	(1.4322 , 1.5929)	0.5836	(0.5321 , 0.6463)
12	1.7330	(1.6535 , 1.8125)	0.5139	(0.4635 , 0.5767)
14	1.7823	(1.6858 , 1.8788)	0.5563	(0.4959 , 0.6335)

Using the estimated values $\hat{\mu}$, respectively $\hat{\sigma}$, at each annealing time $t \in \{2,4,6,8,10,12,14\}$, we found by linear regression the following laws of evolution for the parameters $\mu(t) = 0.05t + 1.0524$ and $\sigma(t) = -0.0046t + 0.6253$, see Figures 14 and 15.

In consequence, the grain growth (GG), can be modelled like a process $\{G_t\}, t \in (0,14)$, where the grain size G_t, at the time *t,* is a random variable having the probability density function:

$$l(g;t) = \frac{1}{(-0.0046t + 0.6253)g\sqrt{2\pi}} \exp\left(-\frac{(\ln g - 0.05t - 1.0524)^2}{2(-0.0046t + 0.6253)^2} \right), \quad \forall x > 0. \qquad \textbf{Eq.3}$$

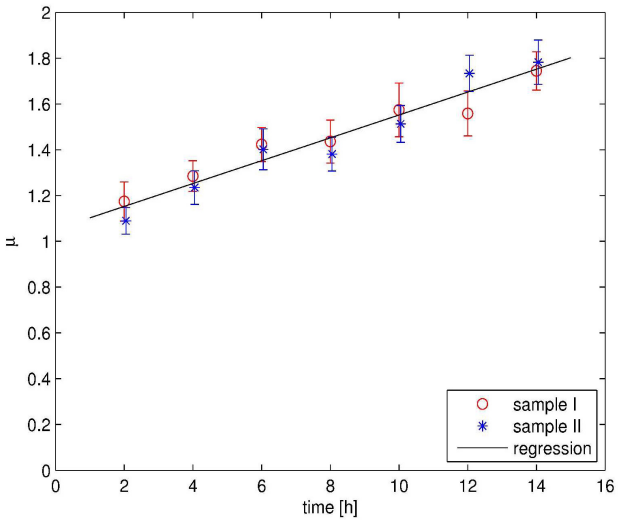

Fig. 14. Estimators of μ and the regression line.

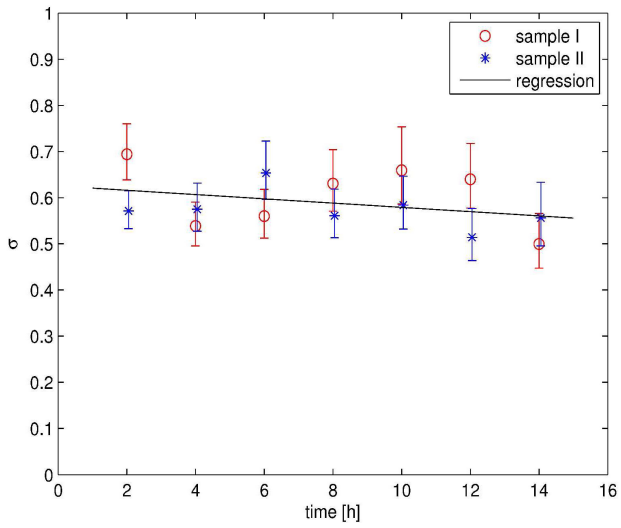

Fig. 15. Estimators of σ and the regression line.

The time evolution of the grain size distribution is shown in Figure 16.

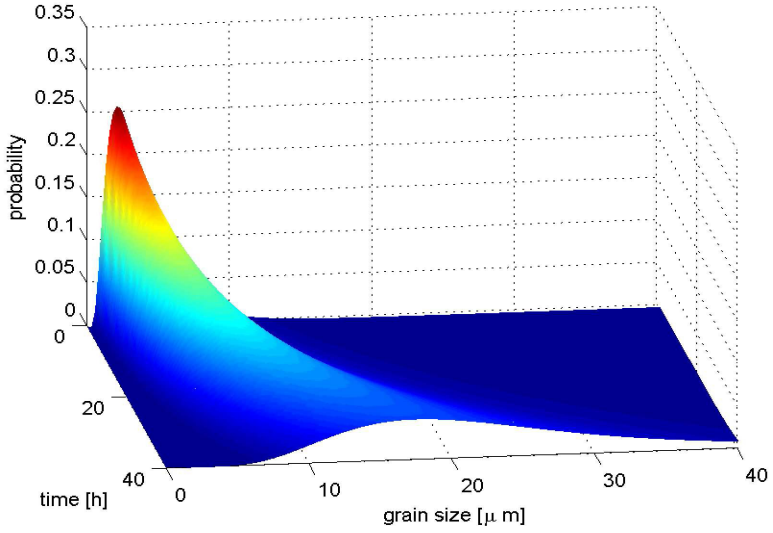

Fig. 16. Distribution of the grain size vs. time for the log-normal model.

3.3.3 The Weibull model

One supposes that, the grain size at each moment *t* is a Weibull random variable having the probability density function f, with parameters λ and k:

$$f(x;\lambda,k)=\frac{k}{\lambda}\left(\frac{x}{\lambda}\right)^{k-1}\exp\left(-\left(\frac{x}{\lambda}\right)^{k}\right),\quad x>0, \qquad \textbf{Eq.4}$$

where $\lambda>0$ is the shape parameter and $k>0$ is the scale parameter.

For each set of the measured grain sizes $X=\{x_i, i=1,2,...,N\}$, at the moment *t*, we calculated the maximum likelihood parameter estimators ($\hat{\lambda}$ and $\hat{k}$) and the 95%-confidence

intervals for λ and k. The values corresponding of the two sample sets are presented in Tables 4 and 5.

Table 4. Maximum likelihood parameter estimators and confidence intervals for sample set I

	Parameter λ		Parameter k	
Time	$\hat{\lambda}(t)$	**Confidence interval 95%**	$\hat{k}(t)$	**Confidence interval 95%**
2h	4.5591	(4.1694 , 4.9852)	1.4576	(1.3359 , 1.5903)
4h	4.7758	(4.4242 , 5.1554)	1.7167	(1.5760 , 1.8700)
6h	5.5259	(5.0920 , 5.9967)	1.7131	(1.5608 , 1.8803)
8h	5.8452	(5.2619 , 6.4932)	1.4945	(1.3450 , 1.6605)
10h	6.8351	(5.9740 , 7.8204)	1.3909	(1.2285 , 1.5747)
12h	6.5564	(5.9298 , 7.2493)	1.6116	(1.4401 , 1.8035)
14h	7.3935	(6.7506 , 8.0976)	1.9279	(1.7148 , 2.1675)

Table 5. Maximum likelihood parameter estimators and confidence intervals for sample set II.

	Parameter λ		Parameter k	
Time	$\hat{\lambda}(t)$	**Confidence interval 95%**	$\hat{k}(t)$	**Confidence interval 95%**
2h	3.9817	(3.7346 , 4.2452)	1.6827	(1.5664 , 1.8076)
4h	4.6470	(4.2554 , 5.0746)	1.5352	(1.4090 , 1.6726)
6h	5.6804	(5.1483 , 6.2675)	1.4611	(1.3283 , 1.6072)
8h	5.3310	(4.8931 , 5.8081)	1.6287	(1.4873 , 1.7836)
10h	6.1135	(5.6097 , 6.6625)	1.6907	(1.5317 , 1.8663)
12h	7.3218	(6.7476 , 7.9449)	1.9943	(1.7829 , 2.2307)
14h	7.9209	(7.1002 , 8.8366)	1.6707	(1.4828 , 1.8825)

Using the estimated values $\hat{\lambda}$, respectively $\hat{k}$, at the time $t \in \{2,4,6,8,10,12,14\}$, we found by linear regression the following laws of evolution for the parameters $\lambda(t) = 0.2766t + 3.6795$ and $k(t) = 0.0178t + 1.4989$, see Figures 17 and 18.

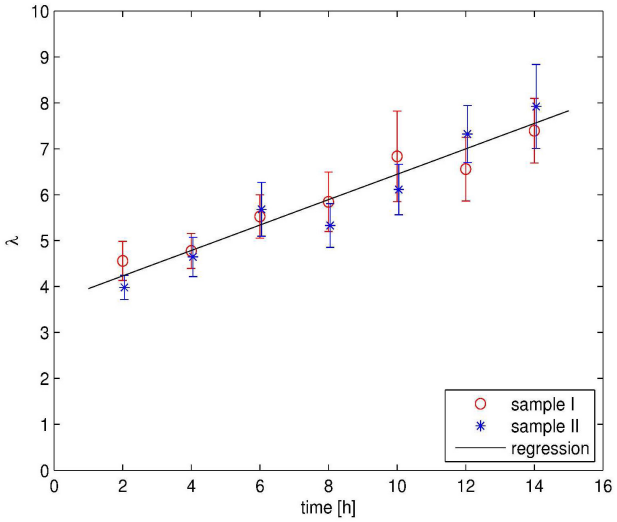

Fig. 17. Estimators of λ and the regression line.

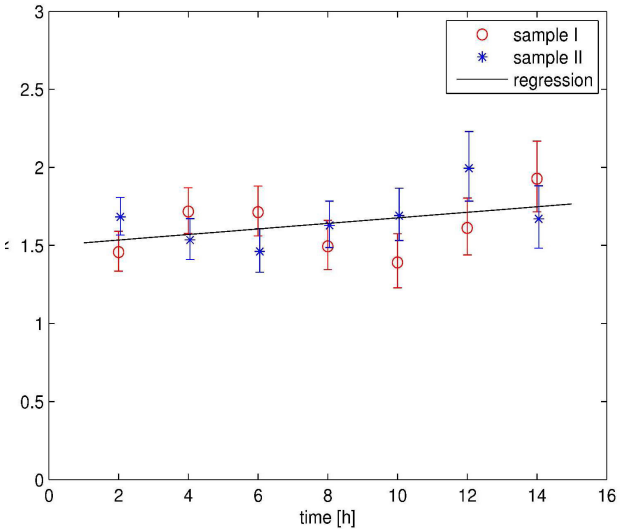

Fig. 18. Estimators of k and the regression line.

In consequence the grain growth is modelled by a process $\{G_t\}, t \in (0,14)$, where G_t is a Weibull random variable having the probability density function:

$$w(g;t) = \frac{k(t)}{\lambda(t)}\left(\frac{g}{\lambda(t)}\right)^{k(t)-1} \exp\left(-\left(\frac{g}{\lambda(t)}\right)^{k(t)}\right), \quad g > 0, \qquad \textit{Eq.5}$$

with $\lambda(t) = 0.2766t + 3.6795$ and $k(t) = 0.0178t + 1.4989$.

The time evolution of the grain size distribution is shown in Figure19.

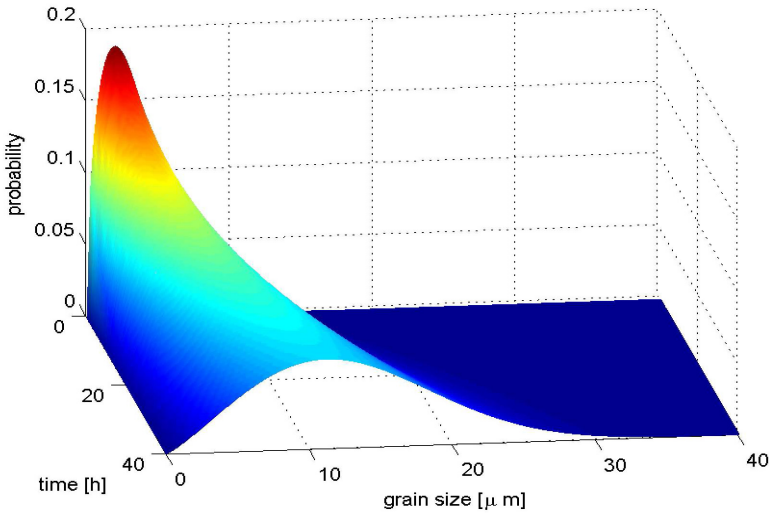

Fig. 19. Distribution of the grain size vs. time for the Weibull model.

Residual impurities and intentionally added doping play a major role in determining the final microstructure of the ceramic support and the related properties of polycrystalline sintered doped alumina. The particular case of 150Y:αAl_2O_3 is even more interesting as the solubility of yttrium in alumina is <10 ppm even at temperatures approaching the melting point of alumina. Due to its low solubility in bulk αAl_2O_3, yttrium is strongly segregated at "special" grain boundaries (e.g. (01-12) plane), [21], causing an improvement of the mechanical properties (e.g. creep resistance). This article was dedicated to the structural evolution of the 150Y:αAl_2O_3

substrate grains, in strong correlation with HA sputtered layers' structure. The experimental reproducibility of the structures, prepared in the same conditions of sintering and annealing, was studied and demonstrated. The morpho-structural investigations and the statistical data analyses suggested a linear time dependence of the grains' size. The very thin (110 – 200 nm) HA sputtered layer, see Figure 4, covered intimately the grains, strongly adhering to the $150Y:\alpha Al_2O_3$ substrate surface. The increase of average value of the grains had not influenced the structure of the $HA/150Y:\alpha Al_2O_3$ system and the compatibility between the HA layer and the doped alumina structures. As reported in some previous works [18–20] the graded buffer layers' (in our case $(Al_2O_3)_x(HA)_{1-x}$ (x=0–1)) role is to attenuate the materials' interface discontinuity, improving the adherence strength.

The main role in the grain growth of $150Y_2O_3:\alpha Al_2O_3$ – **I** & **II** could be attributed to the porosity and the segregation of the Y dopant on the grain boundaries. Two mathematical models for the grain growth were proposed using random variable for the grain size at each time: the *log-normal model* and the *Weibull model*. The model based on *Weibull distributions* fits better the experimental data than *log-normal model*.

4. Conclusions

A new $HA/Y_2O_3:\alpha Al_2O_3$ system was successfully obtained by the deposition of a hydroxyapatite thin layer (~150 nm), by magnetron sputtering, onto sintered substrates of low yttria (150 ppm) doped alumina. The grains shape of the $150Y:\alpha Al_2O_3$ support is polyhedral, with sharp edges. The HA sputtered films layer covered the doped alumina edged surface entirely, the shape of the HA covered grains becoming polyhedral with round edges. The morphology of the layers was homogeneous, while at the HA / $Y_2O_3:\alpha Al_2O_3$ interface no loosening phenomena were evidenced. The grains' size had a linear increase with the annealing time. Both proposed mathematical models (*the log-normal model* and the *Weibull model)* demonstrated the reproducibility of the processes and the linear increase of the grains' size.

Acknowledgments: The authors gratefully acknowledge the financial support of PN09-450102 and PN II 71-031/2007 projects. Thanks are due to A. Ion for preparation of the TEM specimens and to Dr. P Nita for SEM analysis assistance.

References

[1] V. A. Dubok, Powder Metall Met. Ceram. **39**, 381 (2000).
[2] B. D. Ratner, A. S. Hoffman, F. J. Schoen, J. E. Lemons, Biomaterials Science: An Introduction to Materials in Medicine, Elsevier Academic Press, London (2004).
[3] R. L. Hentrich, G. A. Graves, H. G. Stein, P. K. Baipai, J. Biomed. Mater. Res. **5**, 25 (1971).
[4] A. Noiri, F. Hoshi, H. Murakami, K. Sato, S. Kawai, K. Kawai, Ganki **53,** 476 (2002).
[5] J. R. T. Jeffers, W. L. Walter, J. Bone Joint Surg.-Br. Vol. **94B**, 735 (2012).
[6] N. Sugano, M. Takao, T. Sakai, T. Nishii, H. Miki, K. Ohzono, J. Arthroplast. **27**, 736 (2012).
[7] G. Maccauro, G. Bianchino, S. Sangiorgi, G. Magnani, D. Marotta, P. F. Manicone, L. Raffaelli, P. Rossi Iommetti, A. Stewart, A. Cittadini, A. Sgambato, Int. J. Immunopathol. Pharmacol. **22**, 773 (2009).
[8] D. Amutha Rani, Y. Yoshizawa, K. Hirao, Y. Yamauchi, J. Am. Ceram. Soc. **87,** 289 (2004)
[9] I. MacLaren, R. M. Cannon, M. A. Gülgün, R. Voytovych, N. Popescu-Pogrion, C. Scheu, U. Täffner, M. Rühle, J. Am. Ceram. Soc. **86**, 650 (2003).
[10] S. Constantinescu, I. Mercioniu, N. Popescu-Pogrion, J. Optoelectron. Adv. Mater. **10**, 3083 (2008).
[11] M. F. Yan, R. M. Cannon, H. K. Bowen, In: Ceramics Microstructures'76, R. M. Fulrath, J.A. Pask (eds.), Westview Press (1977), pp. 276-307.

[12] N. Popescu-Pogrion, R. Bercia, M. Tirnovan, J. Optoelectron. Adv. Mater. **6**, 1071 (2004).
[13] N. Popescu-Pogrion, I. Mercioniu, R. Bercia, M. Craiu, S. Constantinescu, Proceedings of MS&T'08, p. 844, (2008).
[14] K. Wasa, M. Kitabatake, H. Adachi, Thin Film Materials Technology: Sputtering of Compound Materials, Noyes Publications, New York (2003).
[15] I. Mercioniu, S. Ciuca, I. Pasuk, A. Slav, C. Morosanu, M. Bercu, J. Optoelectron. Adv. Mater. **9**, 2535 (2007).
[16] A. M. Thompson, K. K. Soni, H. M. Chan, M. P. Harmer, D. B. Williams, J. M. Chabala, R. Levi-Setti, J. Am. Ceram. Soc. **80**, 373(1997).
[17] C. A. Handwerker, P. A. Morris, R. L. Coble, J. Am. Ceram. Soc. **72**, 130 (1989).
[18] G. E. Stan, D. Bojin, U.P.B. Sci. Bull. - Series B **72**, 187–196 (2010).
[19] G. E. Stan, A. C. Popescu, I. N. Mihailescu, D. A. Marcov, R. C. Mustata, L. E. Sima, S. M. Petrescu, A. Ianculescu, R. Trusca, C. O. Morosanu, Thin Solid Films **518**, 5955 (2010).
[20] L. E. Sima, G. E. Stan, C. O. Morosanu, A. Melinescu, A. Ianculescu, R. Melinte, J. Neamtu, S. M. Petrescu, J. Biomed. Mater. Res. - Part A **95**, 1203 (2010).
[21 S. Constantinescu, I. Mercioniu, N. Popescu-Pogrion, J. Optoelectron. Adv. Mater. **10**, 3083 (2008).
[22] M. F. Yan, R. M. Cannon, H. K. Bowen, U. Chowdhry, Mater. Sci. Eng. **60**, 275(1983).